Development of a high-precision *XYZ* translator and estimation of beam profile of the vacuum ultraviolet and soft X-ray undulator beamline BL-13B at the Photon Factory

Yoshihiro Aiura,[a]* Kenichi Ozawa,[b,c] Kazuhiko Mase,[c,d] Makoto Minohara[a] and Satoshi Suzuki[e]
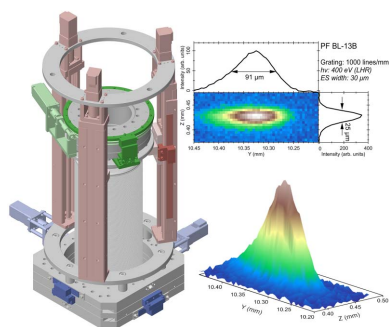
[a]Research Institute for Advanced Electronics and Photonics, National Institute of Advanced Industrial Science and Technology (AIST), Tsukuba, Ibaraki 308-8568, Japan, [b]Department of Chemistry, Tokyo Institute of Technology, Meguro, Tokyo 152-8551, Japan, [c]Institute of Materials Structure Science, High Energy Accelerator Research Organization (KEK), Tsukuba, Ibaraki 305-0801, Japan, [d]SOKENDAI (The Graduate University for Advanced Studies), Tsukuba, Ibaraki 305-0801, Japan, and [e]ExPP Co. Ltd, Tsuchiura, Ibaraki 300-0066, Japan.
*Correspondence e-mail: y.aiura@aist.go.jp

A high-precision *XYZ* translator was developed for the microanalysis of electronic structures and chemical compositions on material surfaces by electron spectroscopy techniques, such as photoelectron spectroscopy and absorption spectroscopy, utilizing the vacuum ultraviolet and soft X-ray synchrotron radiation at an undulator beamline BL-13B at the Photon Factory. Using the high-precision translator, the profile and size of the undulator beam were estimated. They were found to strongly depend on the photon energy but were less affected by the polarization direction. To demonstrate the microscopic measurement capability of an experimental apparatus incorporating a high-precision *XYZ* translator, the homogeneities of an SnO film and a naturally grown anatase TiO_2 single crystal were investigated using X-ray absorption and photoemission spectroscopies. The upgraded system can be used for elemental analyses and electronic structure studies at a spatial resolution in the order of the beam size.

1. Introduction

Understanding the microscopic dynamics of electrons/holes in solids is essential, not only for improving the functionality of existing electronic devices but also for developing new innovative technologies. Angle-resolved photoemission spectroscopy (ARPES) utilizing synchrotron radiation is a powerful and attractive tool for directly studying the microscopic dynamics of electrons/holes (Hüfner, 2003). In ARPES, the microscopic dynamics of electrons, such as the band structure and Fermi surface, are extracted by measuring the energy and emission angle of the photoelectrons emitted from the surface. With significant improvements in the energy and angular resolutions of energy analyzers, a precise angle control of samples is strongly desired (Damascelli *et al.*, 2003; Hüfner, 2007). To precisely and fully control the angle of samples, we developed a two-axis cryogenic sample goniometer that can control the azimuth/tilt angles (Aiura *et al.*, 2003) and a rotary feedthrough that can control the polar angle (Aiura & Kitano, 2012). Recently, a rotatable high-resolution ARPES system for tunable linear-polarization geometries (Iwasawa *et al.*, 2017*a*) and a laser-based ARPES system (Iwasawa *et al.*, 2017*b*) incorporating the sample goniometer and the rotary feedthrough have been developed.

Many of the interesting chemical/physical properties of materials often stem from the spatially inhomogeneous electronic structures at the micro/nano-scale, such as correlated materials that exhibit phase separation (Iwasawa *et al.*, 2019; Lupi *et al.*, 2010; Kondo *et al.*, 2007), active catalysts on irregular surfaces (Zeradjanin *et al.*, 2014; Picone *et al.*, 2016), two-dimensional layers of transition-metal chalcogenides (Liu *et al.*, 2018), micro/nano-crystallites embedded in host materials (Lee *et al.*, 2017), electronic functional organic microcrystalline materials (Lee *et al.*, 2018; Sumi *et al.*, 2019; Zhang *et al.*, 2019), heterogeneous catalysts for organic synthesis (Grätzel, 2009) and micro/nano-engineered thin devices (Picone *et al.*, 2016; Fukuda & Someya, 2017). To study such local electronic structures, micro/nano-scale scanning microscopy measurements are desired, not only for ARPES but also for high-resolution photoemission spectroscopy (HRPES) and X-ray photoemission spectroscopy (XPS) (Günther *et al.*, 2002; Dudin *et al.*, 2010; Avila *et al.*, 2013; Rotenberg & Bostwick, 2014; Hoesch *et al.*, 2017; Iwasawa *et al.*, 2017*a*,*b*, 2018; Jacobsen, 2019). Scanning microscopy technologies using synchrotron light sources have been actively developed. To perform scanning microscopy measurements by ARPES/HRPES/XPS, it is vital to improve the precision of sample position control and reduce the beam size at the sample position.

We have been improving/upgrading the apparatus installed on the vacuum ultraviolet and soft X-ray (VUV/SX) undulator beamline, BL-13B, at the Photon Factory (PF BL-13B) to enable scanning microscopy measurements. To precisely control the sample position, we developed a high-precision *XYZ* (HP-*XYZ*) translator and evaluated its performance. We then evaluated the beam profile using this translator. The beam profile and size strongly depend on the photon energy but are less affected by the polarization direction. The beam position varies with the photon energy and polarization direction. Finally, to demonstrate the performance of the upgraded apparatus at PF BL-13B, the homogeneities in a stannous oxide (SnO) film and a naturally grown anatase titanium dioxide (a-TiO$_2$) single crystal were investigated using X-ray absorption and photoemission spectroscopies. The results suggest that the upgraded apparatus can be used for elemental analyses and electronic structure studies at a spatial resolution in the order of the beam size.

2. High-precision *XYZ* translator

To perform ARPES measurements, we developed a two-axis cryogenic sample goniometer that can precisely control the azimuth/tilt angles of samples (Aiura *et al.*, 2003). For an easy and flexible installation of two driving systems (for azimuth and tilt rotations) and a cryostat into the sample goniometer, an ICF152-series mounting flange was used. To linearly move the goniometer, a wide-bore translator was required. Fig. 1 shows a conventional (commercially available) wide-bore translator used to move large objects, such as the sample goniometer, in and out of a vacuum system (conventionally defined as the *Z* axis). The *Z* motion is driven by three linear
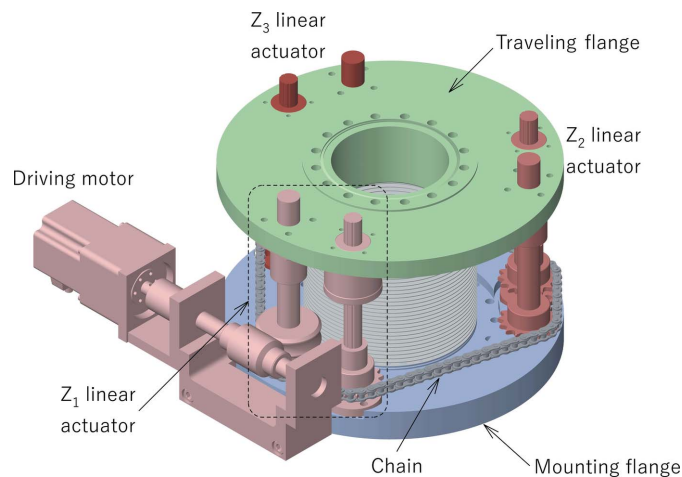

Figure 1
Conventional *Z* linear translator.

actuators comprising a ball screw and a linear guide, which are linked by a driving chain. Because of mechanical problems, such as chain elongation, looseness and roughness, it is not possible to drive the three linear actuators in full synchronization even if a chain tensioner mechanism is installed in the *Z* translator. The slight time lag in each linear actuator causes an irregular fluctuation in the traveling flange during the *Z* motion and a fluctuation in the sample position in the horizontal plane perpendicular to the *Z* axis. Therefore, a conventional wide-bore translator cannot be used for experiments that require precise position control in, for example, micro/nano-scale scanning microscopy measurements.

By attaching driving motors to each of the three linear actuators and moving them synchronously, we can eliminate the fluctuation in the traveling flange during the *Z* motion. We developed a HP-*XYZ* translator, as shown in Fig. 2, that incorporates three independent linear drive units for *Z*-axis motion (iXYZ, ExPP Co. Ltd). The drive unit consists of a linear actuator with a lead of 4 mm (KR3304, THK Co. Ltd) and a stepping motor incorporating a harmonic gear with a reduction ratio of 100 (AZM24AK-HS100, Oriental Motor Co. Ltd). Since we do not require the chain used in the conventional *Z* translator, the drive transmission efficiency and accuracy are drastically improved. Hence, the traveling flange can be precisely translated by relatively small motors. The developed HP-*XYZ* translator is made more compact than the conventional one by downsizing the driving motors. Moreover, the traveling flange is mounted on the linear actuators via balls, as shown in the enlarged view of Fig. 2, making it possible to adjust the inclination of the traveling flange by driving the motors independently. The basic resolution of the stepping motors is set at 10 000 pulses revolution^{-1} (p r^{-1}); this corresponds to a total resolution of 1 000 000 p r^{-1} including the harmonic gear. Therefore, the nominal traveling resolution along the *Z* axis is 4 nm. For *X*/*Y* motions in the plane perpendicular to the *Z* axis, commercially available ball screws with a lead of 2 mm are used (BNK0802, THK Co. Ltd). Since the same stepping motors as those in the *Z* actuators are used, the nominal traveling resolutions along

the *X* and *Y* axes are the same, *i.e.* 2 nm. The travel *X*/*Y* and *Z* distances of the HP-*XYZ* translator are ±15 mm and 260 mm, respectively. The HP-*XYZ* translator along with a high-precision rotary feedthrough developed previously (Aiura & Kitano, 2012) is attached to the apparatus installed at PF BL-13B (Toyoshima *et al.*, 2013).

Owing to the significantly reduced fluctuation in the traveling flange, it was possible to attach an absolute fine-pitch optical encoder system with a resolution of 1 nm (RESOLUTE, Renishaw) onto the HP-*XYZ* translator. To measure the positions of the *X*/*Y* axes precisely, the same high-precision encoder systems as in the *Z*-axis one were attached. To reduce the effect of temperature variation under actual measurement environments, linear scales made of a nickel–iron alloy with a low thermal expansion were used (RELA, Renishaw). The encoder positions are read on a personal computer via an encoder counter that was recently developed and made commercially available (ER4C-BiSS, Tuji Electronics Co. Ltd). Since the encoder counter has limit outputs that can help arbitrarily set the limit values, the absolute encoders can also work as flexible limiters for motor control, independent of the personal computer. To improve the reading accuracy, the encoder counter can read the integrated value of the position measured any number of times between 1 and 1000.

Since the actual positions could be read accurately by the absolute encoders, the performance of the HP-*XYZ* translator could be quantitatively evaluated. Fig. 3 shows the actual positions measured by the encoder and the travel-distance deviations as a function of the nominal positions estimated based on the pulse number of the motors (see Figs. S1 and S2 in the supporting information for all datasets). As indicated by the deviations (red) in the upper three panels 3(*a*)–3(*c*), fluctuations in one revolution of the screw shaft can be seen for the *X*/*Y* axes (2 mm lead intervals); however, the fluctuation for the *Z* axis (4 mm lead interval) is not significant. The lower fluctuation for the *Z* axis is presumed to be owing to the averaging of the fluctuations of the three mounted linear actuators. With the
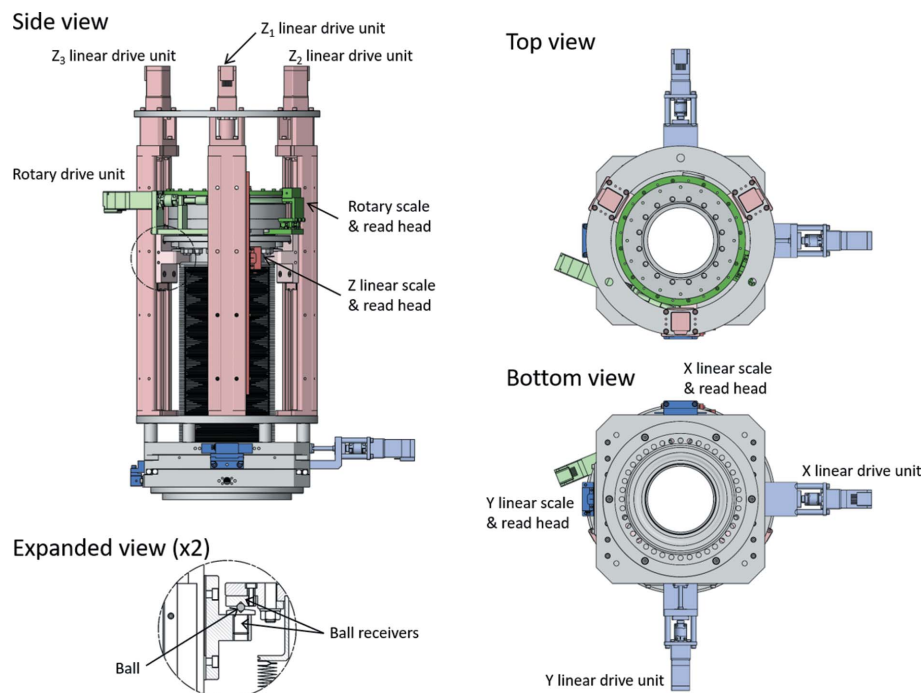

Figure 2
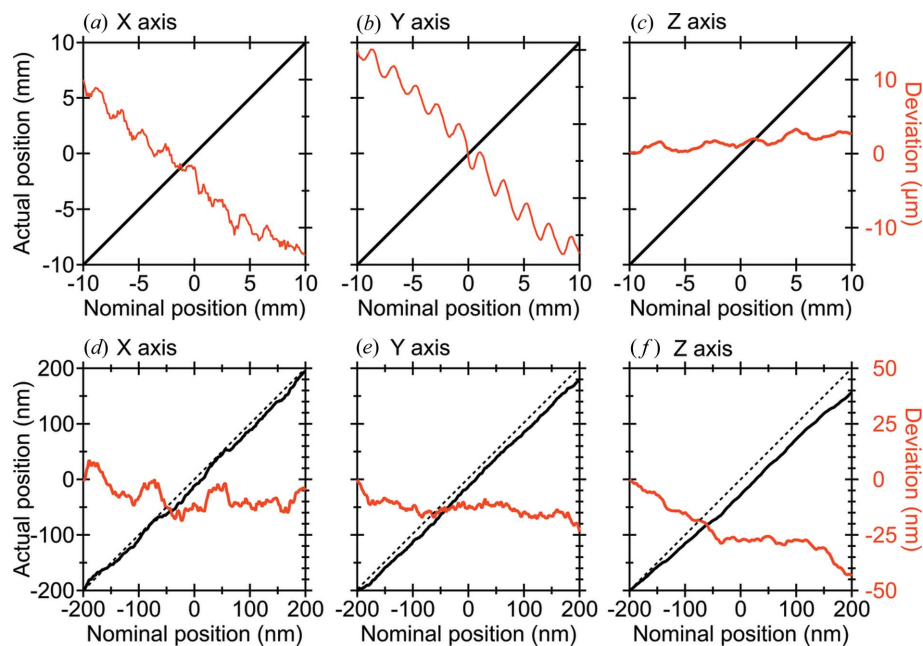HP-*XYZ* translator and high-precision rotary feedthrough (Aiura & Kitano, 2012).

Figure 3
Actual positions (black) and travel-distance deviations (red) along the (*a*) *X* axis, (*b*) *Y* axis and (*c*) *Z* axis as a function of the nominal position. The deviation is the difference between the actual position read by the encoder and the nominal position estimated based on the pulse number of the stepping motors. The actual positions are measured in the range from −10 to +10 mm at nominal intervals of 0.1 mm. The figures (*d*), (*e*) and (*f*) are the same as (*a*), (*b*) and (*c*), respectively; however, the measurements are made at the nominal interval of the motor traveling resolution (2 nm and 4 nm for the *X*/*Y* and *Z* axes, respectively). The actual position is the average of the integrated values obtained by measuring the encoder position 1000 times.
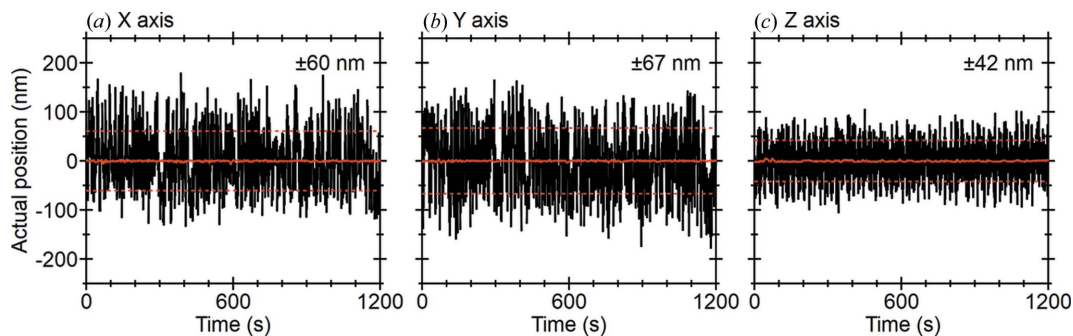
Figure 4
Elapsed-time dependency of encoder positions in the (*a*) *X* axis, (*b*) *Y* axis and (*c*) *Z* axis. The red lines indicate the average of the integrated values obtained by measuring the encoder position 1000 times. The motors are controlled such that the average position remains at the original one. The red broken lines indicate the SDs of the non-averaged encoder positions.

averaging of the actual position and reduction in reading fluctuation, the linearity between the actual and nominal positions is maintained, even when measured at the nominal interval of the motor traveling resolution, as shown in panels 3(*d*)–3(*f*). This suggests that the HP-*XYZ* translator can be controlled at the motor traveling resolution (2 nm and 4 nm for *X*/*Y* and *Z* axes, respectively).

Under the actual measurement environment at PF BL-13B, the *XYZ* positions are affected by external factors, such as the temperature, vibrations, electronic noise and constant fluctuations even when the motors are not driven, as shown in Fig. S3. To eliminate the position drift caused by the external factors and estimate the reading fluctuation/accuracy, the motors were feedback controlled so that the reading position remained at the original one. Fig. 4 shows the actual positions measured as a function of the elapsed time. The *XYZ* positions (black) fluctuated in the order of tens of nanometres because of the influence of the external factors. To reduce/eliminate the reading fluctuation caused by the external factors, the positions were measured 1000 times and averaged (red). The averaged position is almost at the original position. From

the standard deviations (SDs) of the encoder positions, the reading fluctuation of the encoder under the actual measurement condition is estimated to be lower than 100 nm. This suggests that the actual positions of the HP-*XYZ* translator can be controlled with an accuracy of less than 100 nm by correcting the deviation between the actual and nominal positions.

To demonstrate the precise position control of the HP-*XYZ* translator, we measured the spatial distribution of the photocurrent caused by synchrotron radiation passing through a precision hole with an aperture diameter of 1 mm (Edmund). Fig. 5(*a*) shows the experimental setup, where the precision hole and an anode plate to measure the photocurrent are mounted on the HP-*XYZ* translator, allowing position control/scanning. The horizontal direction of the precision hole is aligned along the *Y* axis of the HP-*XYZ* translator and the incident direction of the synchrotron radiation is aligned along the *X* axis. Fig. 5(*b*) shows the optical image of the hole. Horizontal linear-polarized synchrotron radiation with a photon energy (*hν*) of 400 eV was used, and the exit-slit (ES) width of the monochromator
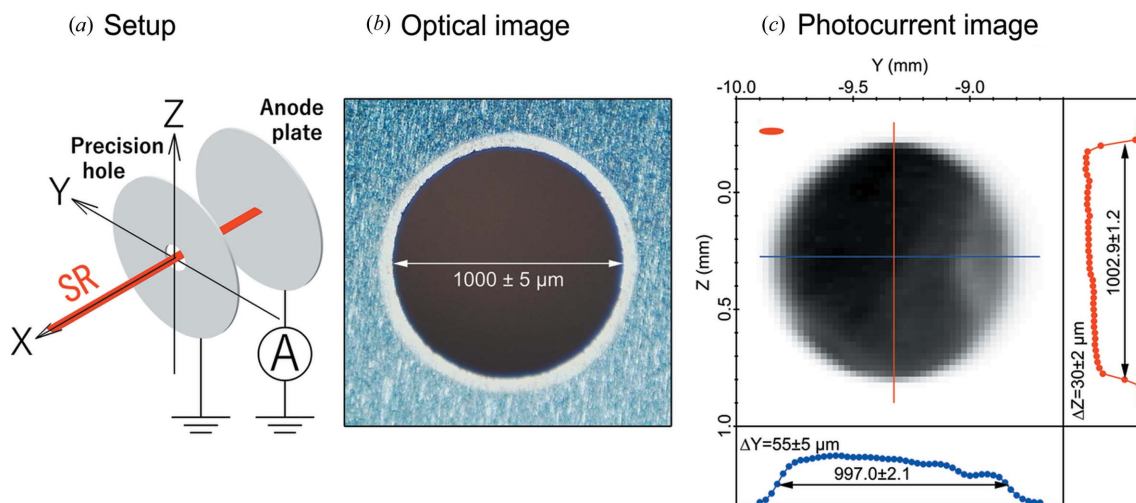

Figure 5
(*a*) Experimental setup for the photocurrent measurement. (*b*) Optical image of precision pinhole with an aperture diameter of 1 mm. (*c*) Spatial distribution of the photocurrent passing through the pinhole. The aperture tolerance of the pinhole is ±5 µm. The red ellipse in the upper left shows the schematic shape of the synchrotron radiation (*hν* = 400 eV, horizontal linear polarized, ES width = 30 µm) at the sample position. The intensity plots along the *Y* axis (blue) and *Z* axis (red) diameter directions are shown in the bottom and right panels, respectively.

was set to 30 µm. At this setting, the beam sizes at the measuring position were estimated to be 91 µm (horizontal) and 25 µm (vertical), as shown in the next section. Fig. 5(c) shows the spatial distribution of the photocurrent. The beam is sufficiently smaller than the hole; thus, the observed photocurrent image accurately reproduces the shape of the hole without any distortion. Here, we would like to emphasize that the observed diameters of the hole in the horizontal (Y) and vertical (Z) axes estimated based on the photocurrent were reproduced within the range of the aperture tolerance. This suggests that the HP-XYZ translator can be used for microscopic measurements in the order of micrometres. The unevenness in the intensity of the photocurrent image [Fig. 5(c)] is assumed to be caused by the contamination of the anode plate. The specifications of the HP-XYZ translator are summarized in Table 1. It should be noted that the fluctuation in the readings or in the accuracy below 100 nm is that of the HP-XYZ translator in air, and not of the sample in vacuum. Based on experimental observations that the actual shape of a precision pinhole could be accurately and quantitively reproduced by the photocurrent image without any distortion (Fig. 5), the position readings of the encoder can be regarded as indicating the actual positions of the sample with an accuracy of a few micrometres or even less.

3. Beam profile at PF BL-13B

The actual beam profile can be assessed by measuring the spatial distribution of the photocurrent passing through a precision pinhole having an aperture diameter sufficiently smaller than the beam size. The setup for the photocurrent measurement is the same as that shown in Fig. 5(a) except for the aperture size of the pinhole with a diameter of 10 µm (Edmund). Through a ray-tracing simulation, the beam size at the sample position, with the ES width set to 40 µm and $h\nu$ set to 100 eV, was estimated to be 130 µm (horizontal) and 40 µm (vertical) (Mase et al., 2010).

Fig. 6 shows the photon-energy dependence of the beam profiles for the ES width set to 30 µm when using (a) 1000 lines mm^{-1} varied-line spacing plane grating (VLSG) and (b) 300 lines mm^{-1} VLSG. The beam size strongly depends on the photon energy. For $h\nu$ = 100 eV and 1000 lines mm^{-1} VLSG, the full width at half-maximum (FWHM) of the beam is estimated to be 216 µm (horizontal) and 53 µm (vertical). Although a focusing postmirror with a vertical magnification ratio of 1:1 was used (Mase et al., 2010), the observed vertical size (53 µm) is

Table 1
Specification of the HP-XYZ translator.

Travel range (XY), (Z) (mm)	±15, 260
Motor resolution (XY) (Z) (nm)	2, 4
Encoder resolution (nm)	1
Reading fluctuation† (nm)	<100

† The encoder positions were estimated under actual measurement conditions at PF BL-13B.

larger than the expected size (30 µm). The observed horizontal size (216 mm) is also larger than the calculated size (130 µm). For $h\nu$ = 400 eV, the beam size is less than half compared with that for $h\nu$ = 100 eV. When the photon energy is further increased to 1000 eV, the beam is blurred again. Interestingly, the peak position of the beam depends on the photon energy.

Fig. 7 shows the beam profiles when using horizontal linear polarization (LHR), vertical linear polarization (LVS), right circular polarization (C+S), left circular polarization (C−S), right elliptical polarization (E+S) and left elliptical polarization (E−S). Although the beam sizes of elliptically polarized synchrotron radiation are slightly larger than those of linear and circularly ones, no significant polarization dependence of the beam size can be observed.

The beam position shifts slightly with the variation in the photon energy (Fig. 6) and polarization state (Fig. 7). Even for the same photon energy and polarization state, since the beam position did not reproduce before and after operating the undulator magnets (see Fig. S4), the observed fluctuation in
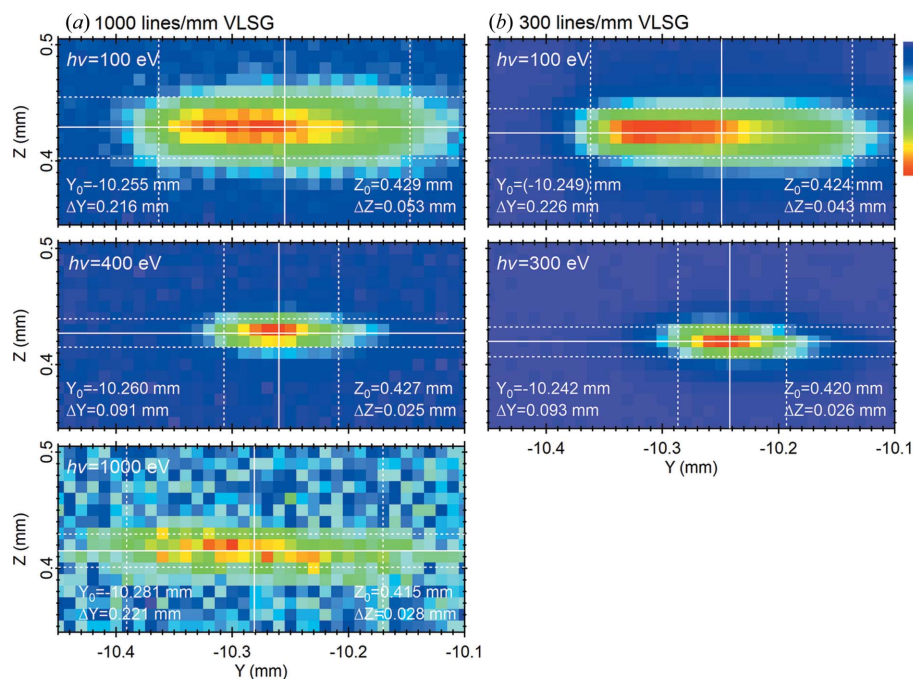

Figure 6
Photon-energy dependence of beam profiles when using (a) 1000 lines mm^{-1} VLSG and (b) 300 lines mm^{-1} VLSG. The ES width is set to 30 µm and the polarization is linear in the horizontal plane. ΔY and ΔZ are the FWHM of the beam intensity along the Y and Z axes, respectively. The dotted lines indicate the position at half-maximum of the beam intensity. Y_0 and Z_0 are the center positions of the beam intensity.
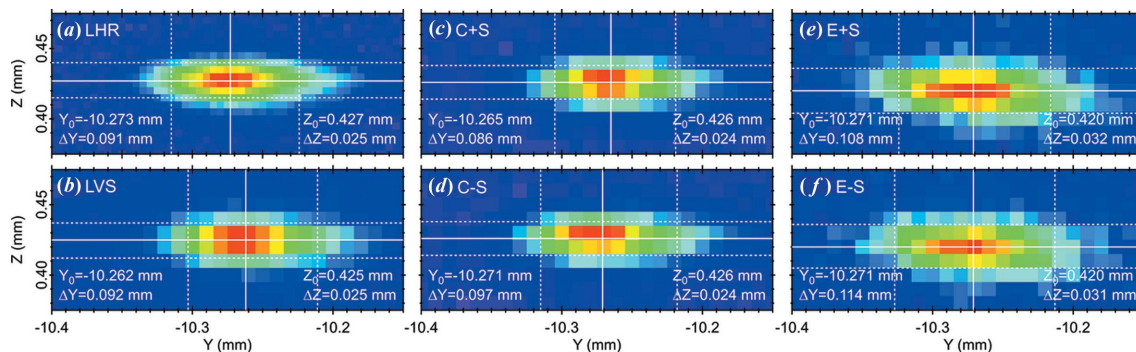
Figure 7
Polarization dependency of the beam profiles when using LHR, LVS, C+S, C−S, E+S and E−S. The ES width and photon energy are set to 30 μm and 400 eV, respectively.

the beam position is not caused by the photon energy or polarization state; it is presumed to be owing to the mechanical reproducibility of the undulator magnets and/or the heat load on the monochromator.

Fig. 8 shows the ES size dependency of the beam profiles. The ES width is the reading (nominal) value of the micrometer. As shown in Fig. 8(e), the integrated intensity along the Y axis increases with the ES size, while the shape remains almost unchanged. On the other hand, the integrated intensity along the Z axis in Fig. 8(d) shows that the width of the curves decreases gradually with decreasing ES size, while the peak intensity remains almost unchanged except for the integrated intensity when the ES width is 10 μm. Fig. 8(b) shows that the FWHM of the integrated intensity along the Z axis (red) is quantitatively proportional to the ES width between 30 and 90 μm, but that along the Y axis (black) is independent of the ES size. As shown in Fig. 8(c), the linear relationship between the total intensity and the ES size is also maintained in the ES width range of 30–90 μm. It seems reasonable to conclude that the deviation when ES = 10 μm is caused by the difference between the nominal (read by the micrometer) and actual ES width values and/or the interplay between the ES size (10 μm) and the aperture size of the pinhole (10 μm).

4. Example measurements using the upgraded apparatus at PF BL-13B

4.1. Composition evaluation of SnO film

To demonstrate the performance of the system incorporating the HP-XYZ translator, the spatial distribution of the absorption coefficient was measured at a fixed photon energy. Using binary oxides is advantageous in terms of controlling the physical properties through the constituent ions. For example, SnO is expected to be a promising
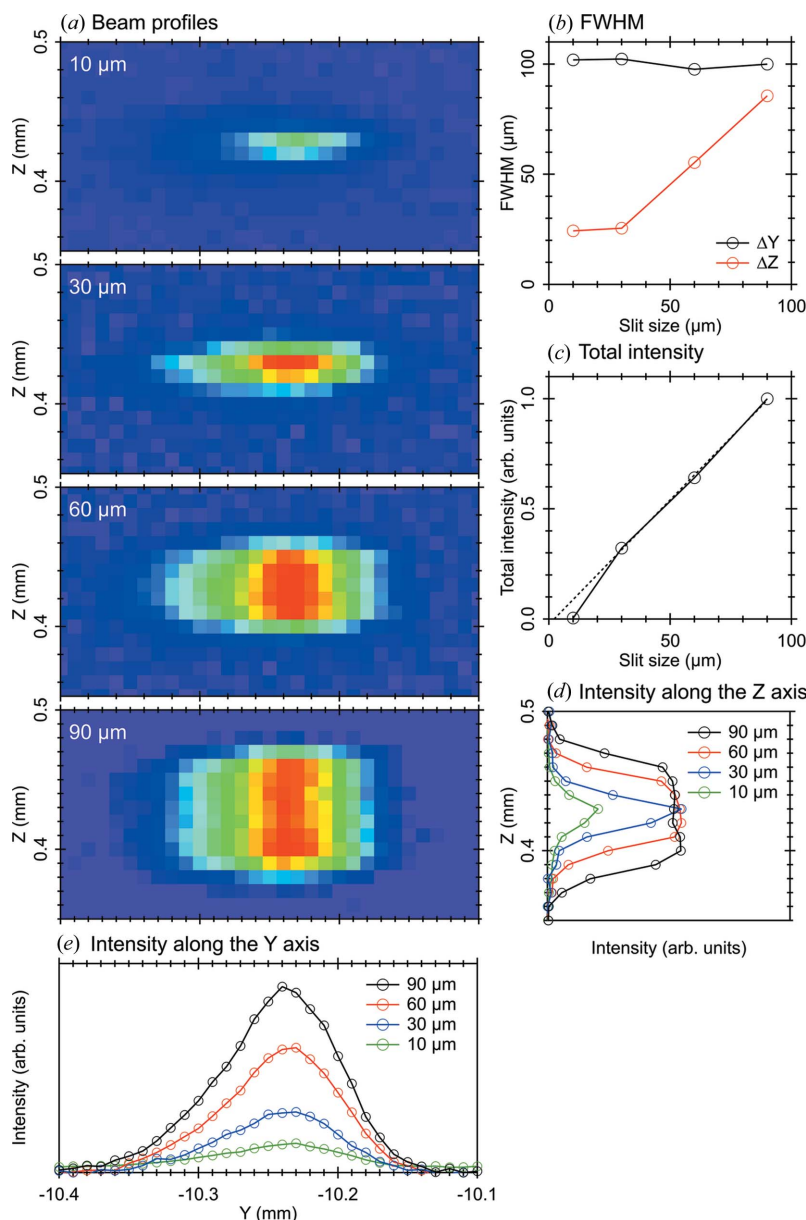

Figure 8
(a) ES size dependency of the beam profiles. The photon energy is set to 400 eV and the polarization is linear in the LHR. (b) Spot size (FWHM) along the Y axis (black) and Z axis (red). (c) Total intensity. (d, e) Integrated intensities along the Z and Y axes, respectively.

material for practical devices as a p-type oxide semiconductor. Recently, we improved the hole mobility of an SnO film by modulating the growth thermodynamics and kinetics (Minohara *et al.*, 2019, 2020).

Fig. 9 shows the X-ray absorption spectroscopy (XAS) spectra of the SnO film grown on an yttrium-doped ZrO_2 (YSZ) (001) substrate, reproduced from those reported previously (McLeod *et al.*, 2012; Quackenbush *et al.*, 2013; Sharma *et al.*, 2016; Minohara *et al.*, 2019). To investigate the compositional homogeneity, the SX was set to be the photon energy corresponding to the characteristic/intense absorbed peak structure near the Sn *M*-edge (487.6 eV) and O *K*-edge (534.2 eV), and the spatial distribution was measured. Figs. 10(*a*) and 10(*b*) show the spatial distributions of the absorption coefficient at photon energies of 487.6 eV and 534.2 eV, respectively, on the entire SnO film with a size of 10 mm × 10 mm. The images show that there are

many small non-uniform structures, referred to as 'voids' hereafter, with sizes less than several hundred micrometres. To study the small voids in detail, we measured the spatial distribution of the absorption coefficient for the area enclosed by the rectangles in panels 10(*a*) and 10(*b*). From the detailed
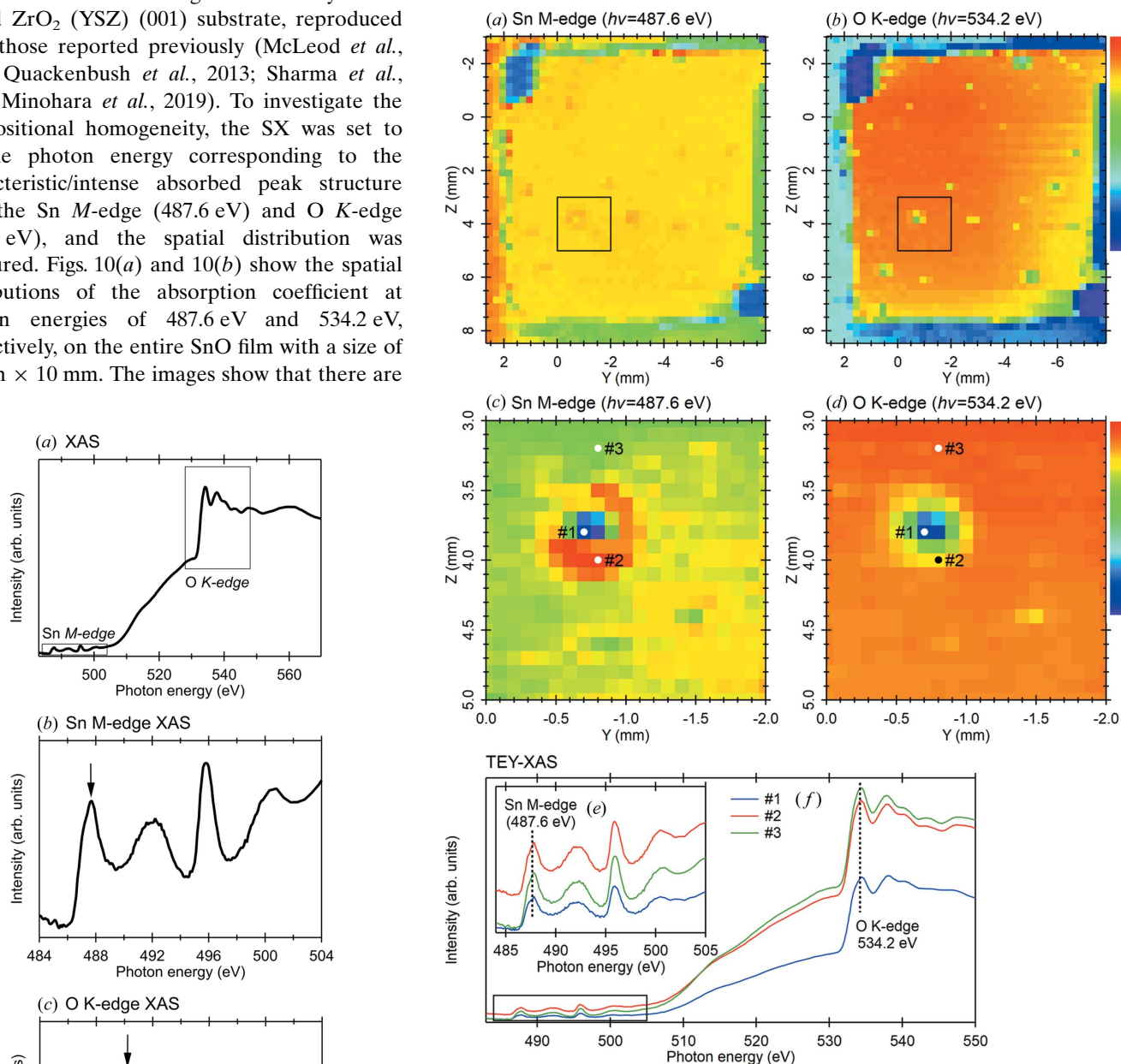

Figure 9
(*a*) XAS spectrum of the SnO film at the homogeneous portion, or at point #3 in Figs. 10(*c*) and 10(*d*). (*b*, *c*) Enlarged views near the Sn *M*-edge and O *K*-edge, respectively. The spectrum is measured using the total electron yield method at room temperature.

Figure 10
(*a*, *b*) Spatial distributions of the absorption coefficient of the SnO film at photon energies of 487.6 eV and 534.2 eV, respectively. The measurements were performed at room temperature. The size of the prepared SnO film is 10 mm × 10 mm. The scan range was set to 10.25 mm and 11.25 mm for the *Y* and *Z* axes, respectively, and the scan interval was set to 0.25 mm. A total of 1932 data points were mapped out with an acquisition time of ~90 min. (*c*, *d*) Spatial distributions of the absorption coefficient for the area enclosed by the rectangles in panels (*a*) and (*b*), respectively. The scan range and interval were set to 2 mm × 2 mm and 0.1 mm, respectively. A total of 441 data points were mapped out with an acquisition time of ~20 min. Since those spatial distributions were measured by scanning the sample, the scanning directions of the *Y* and *Z* axes are opposite to the actual directions in the real space. Therefore, the images were plotted in a descending order. (*e*, *f*) XAS spectra at positions #1 (blue), #2 (red) and #3 (green) for the Sn *M*-edge and O *K*-edge as indicated in panels (*c*) and (*d*), respectively.

Aiura *et al.* • An *XYZ* translator and the beam profile of the BL-13B beamline   **929**

spatial distribution in panels 10(c) and 10(d), it can be seen that the voids exhibit a complex shape and not a simple point shape. To investigate the cause of the drastic change in intensity around the voids, the XAS spectra were measured at the center [#1 in panels 10(c) and 10(d)] and edge (#2) of the void, and were compared with the XAS spectra at the uniform position (#3). Figs. 10(e) and 10(f) show the XAS spectra near the Sn M-edge and O K-edge, respectively, at those positions. The blue, red and green lines correspond to the XAS spectra at the positions #1, #2 and #3, respectively. The intensity in the XAS spectra near the Sn M-edge and O K-edge significantly decreases at the center of the void (blue). This suggests that the Sn and O compositions around the void are lower than those at the other positions. On the other hand, the absorption coefficient near the Sn edge increases significantly around the edge of the void [#2 position in Fig. 10(c)]. From the XAS spectra [Fig. 10(e)], it can be seen that the observed increment is not caused by the increase in the intrinsic absorption coefficient owing to Sn and O but caused by the increase in the background intensity. To fabricate micrometre-order oxide devices using the SnO film and/or to further improve the semiconductor characteristics of the SnO film, it is necessary to clarify the origin of the voids and find methods to control/eliminate them. Our microscopy system incorporating the HP-XYZ translator will be very useful as a film evaluation technique.

Figure 11
(a) Experimental setup for the PES measurement and an overview image of the naturally grown a-TiO$_2$ single crystal. (b) Spatial distribution of the spectral intensity around Ti 2p region on the (101) surface taken at room temperature with a photon energy of 753 eV. The scan range indicated by the red rectangle in panel (a) was set to 5 mm and 6.4 mm for the Y′ and Z axes, respectively, and the scan interval was set to 0.2 mm. A total of 858 data points were mapped out with an acquisition time of 55 min. (c) Survey PES spectra at the portions indicated by the circles in panel (b). All spectra were recorded at room temperature using a photon energy of 753 eV (LHR).

4.2. Homogeneity evaluation of naturally grown a-TiO$_2$ single crystal

To demonstrate the usefulness and measurement tips of scanning PES by means of the upgraded apparatus at PF BL-13B, the homogeneity of a naturally grown a-TiO$_2$ single crystal was studied. As shown in Fig. 11(a), the naturally grown a-TiO$_2$ single crystal (SurfaceNet GmbH) consisting of two different planes, a (101) plane and a (001) plane, was used. In the study, the photoelectrons emitted from the (101) plane were measured. A clean surface was obtained by cycles of Ar$^+$ ion sputtering followed by annealing, as conventionally used (Ozawa et al., 2018). The experimental setup for this process is described in detail in the literature (Toyoshima et al., 2013). The electron-energy analyzer was placed at 65° with respect to the incoming synchrotron radiation. The sample was placed so that the (101) surface faced the analyzer to collect the photoelectrons emitted along the [101] direction. Here, we define the direction from the sample to the analyzer as the X′ axis, and the horizontal direction within the (101) surface perpendicular to the X′ axis as the Y′ axis.
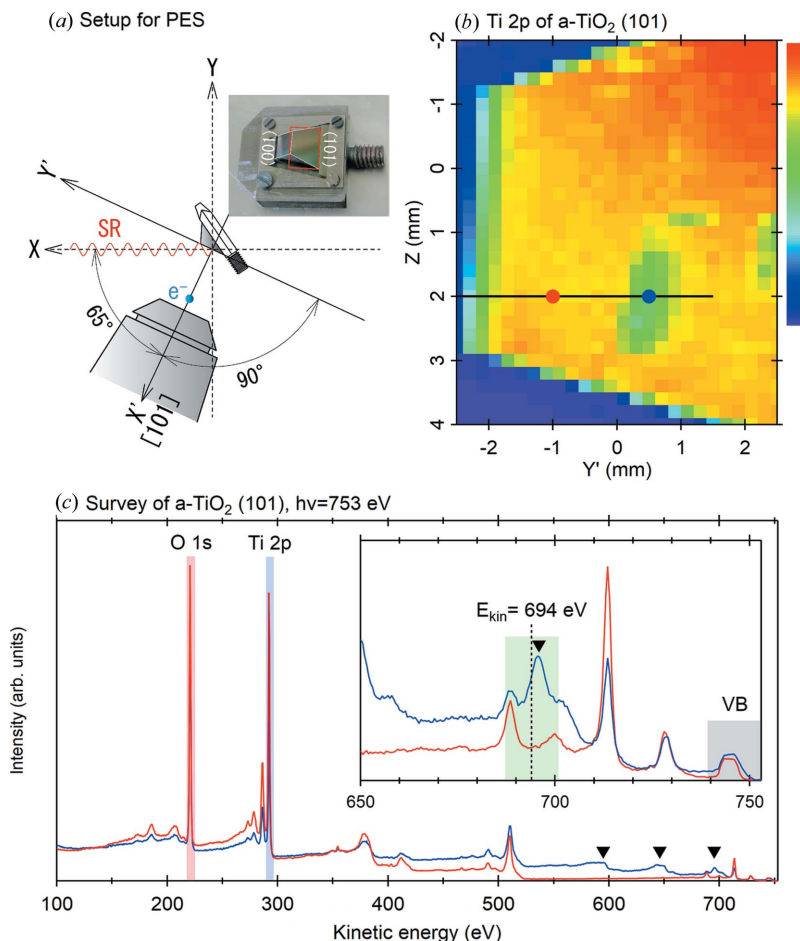
Fig. 11(b) shows the spatial distribution of the spectral intensity around the Ti 2p region on the a-TiO$_2$(101) surface. The spectral intensity was obtained by integrating the photoelectrons emitted in the kinetic energy region shown by the rectangle around the Ti 2p edge in panel 11(c). The observed photoelectron image accurately reproduces the shape of the (101) surface. However, it should be noted that the image is not homogeneous within the (101) surface and that there are some portions where the intensity drops abruptly. Since the X′ distance between the sample and the analyzer, i.e. the focal length, was kept constant in the measurement, the observed abrupt drop in the Ti 2p spectral intensity is caused by the intrinsic inhomogeneity of the naturally grown a-TiO$_2$ single crystal. As shown in the wide-scan (or survey) PES spectra [Fig. 11(c)], all characteristic Ti and O core spectral intensities around the portion where the Ti 2p spectral intensity drops abruptly (blue line) are drastically weakened compared with that at the homogeneous portion (red line). Moreover, it should be noted that the
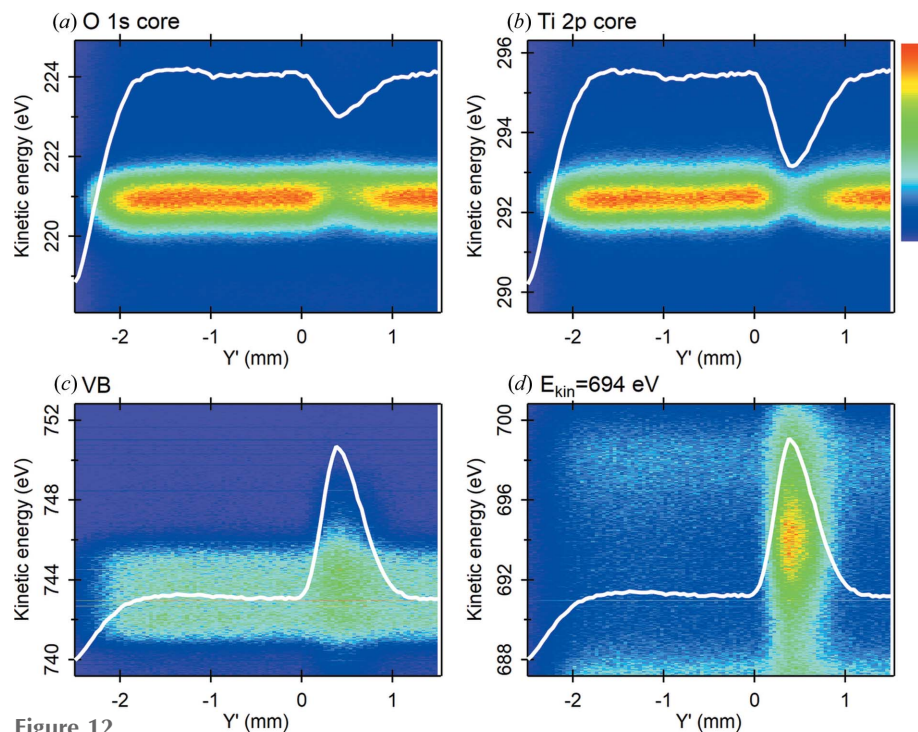
Figure 12
EDC images around (*a*) the O 1*s* core, (*b*) the Ti 2*p* core, (*c*) the valence band and (*d*) a kinetic energy of 694 eV, taken at room temperature with a photon energy of 753 eV. The images were measured by fixing the *Z* axis at 2 mm and scanning the *Y′* axis from −2.5 to 1.5 mm [the black line in Fig. 11(*b*)] at intervals of 0.04 mm. The measured energy ranges correspond to the colored rectangles in Fig. 11(*c*). The white lines were obtained by integrating all photoelectrons emitted in the measured kinetic energy. All spectra were taken at room temperature with a photon energy of 753 eV (LHR).

and by counting only photoelectrons emitted in the direction of an electron-counting detector. The electron-counting detector is composed of a retarding mesh, a microchannel plate and an anode plate (Fujita & Mase, 2007). Since, in this study, the retarding mesh was grounded, all photoelectrons emitted in the direction of the detector were captured. The spatial distribution of the Ti *L*-edge absorption coefficient in the TEY mode [Fig. 13(*c*)] reproduces well that of the Ti 2*p* core [Fig. 11(*b*)]. In addition, the TEY-XAS intensity profile [black lines in Figs. 13(*b*) and 13(*c*)] along the same spatial line as the one measured by the PES is very similar to the corresponding PES spectral shape [white lines in Figs. 12(*a*) and 12(*b*)]. As shown in Figs. 13(*d*) and 13(*e*), the same tendency was displayed in the XAS intensity obtained by the detector. Since the detector was placed under the sample as shown in Fig. 13(*a*), among all photo-electrons emitted from the sample, only the ones grazing the surface were detected. Considering the short mean-free path of the photoelectrons in the solid (Powell, 1988), the XAS spectra of the photoelectrons obtained by the detector are considered to reflect the electronic state near the surface compared with the TEY-XAS spectra (Ozawa *et al.*, 2011; Amemiya, 2012). Therefore, the scanning XAS spectra with different surface sensitivities in Fig. 13 suggest that the impurities are intrinsic in the bulk of the naturally grown a-TiO$_2$ single crystal used in the study.

5. Conclusions and future direction

To enable microscopic measurement with the apparatus installed at PF BL-13B, we developed an HP-*XYZ* translator. The actual positions were controlled with an accuracy (reading fluctuation) of 100 nm or less by continuously correcting the positions using high-precision absolute encoders. With the averaging of the reading positions to reduce the reading fluctuation, the averaged positions were controlled with an accuracy of approximately the resolution of the motors (2 nm for the *X*/*Y* axes and 4 nm for the *Z* axis). Using the HP-*XYZ* translator, we evaluated the beam profile of VUV/SX at PF BL-13B. The beam profile and size depend strongly on the photon energy but are less affected by the polarization direction. The beam size at the sample position for a photon energy of 400 eV (LHR) and an ES size of 30 μm was esti-mated to be 91 μm (horizontal) and 25 μm (vertical). When the photon energy was decreased to 100 eV (LHR), the beam size in the horizontal plane increased to 216 μm. The observed
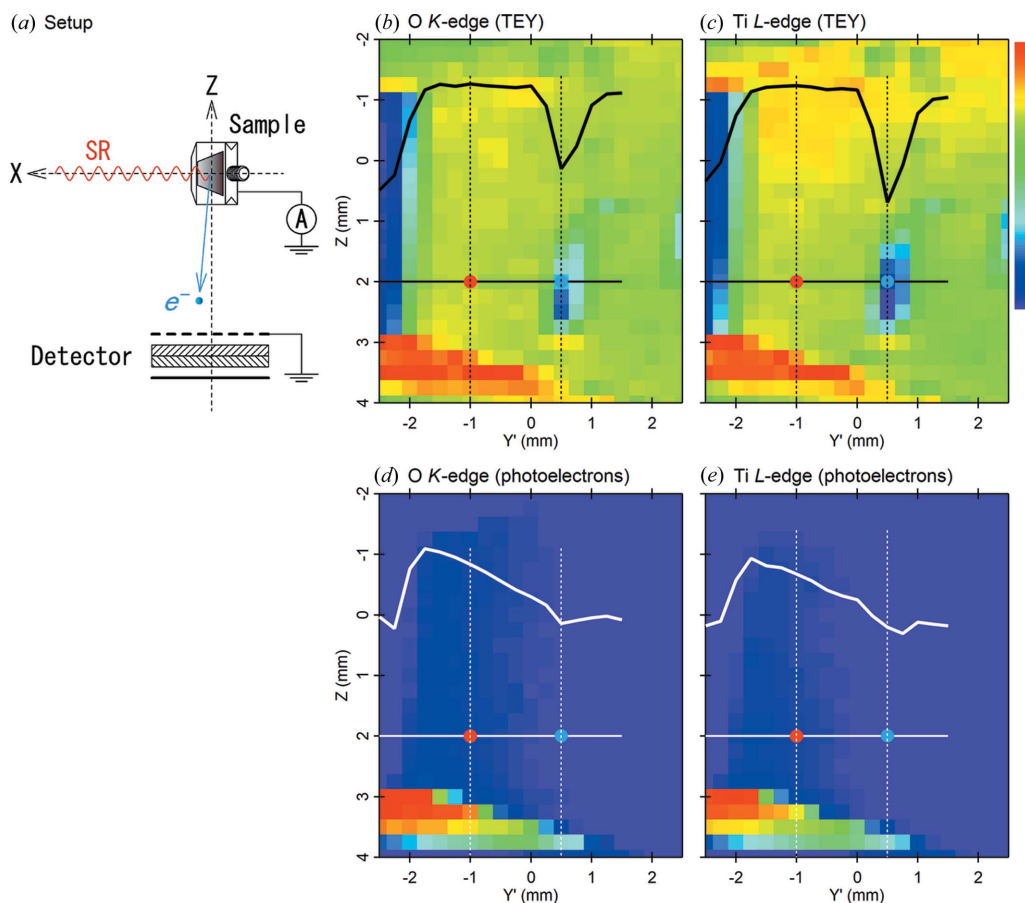
extrinsic core peaks appear around kinetic energies of 590, 645 and 695 eV (shown by the triangles) for the inhomogeneous portion.

To investigate the electronic/compositional characteristics more quantitatively, the electronic distribution curve (EDC) images were measured across the inhomogeneous portion. As shown in Figs. 12(*a*) and 12(*b*), the spectral intensities of Ti 2*p* core and O 1*s* core drop abruptly in the inhomogeneous portion, but the drop in Ti 2*p* core intensity is larger than that in the O 1*s* core. In contrast, the spectral intensities on the high kinetic energy side (or the low binding energy side) are enhanced abruptly in the vicinity of the inhomogeneous portion [Figs. 12(*c*) and 12(*d*)]. As shown from the inset of Fig. 11(*c*), the enhancement in spectral intensity around the valence band [Fig. 12(*c*)] and that around the kinetic energy of 695 eV [Fig. 12(*d*)] are caused by an increase in background intensity and the appearance of an extrinsic peak, respectively. The results suggest that an impurity other than the intrinsic Ti and O is present in the vicinity of the inhomogeneous portion.

The influence of impurities on the PES spectra should be reflected in the XAS spectra. Fig. 13 shows the spatial distri-butions of the absorption coefficient of the naturally grown a-TiO$_2$ single crystal taken at photon energies corresponding to the characteristic O *K*-edge absorption (531.2 eV) and Ti *L*-edge absorption (458.4 eV). The images were obtained by measuring the sample drain current caused by all photoelec-trons emitted from the sample (total electron yield, TEY)

Aiura *et al.* • An *XYZ* translator and the beam profile of the BL-13B beamline   **931**

research papers

Figure 13
(*a*) Experimental setup for the XAS measurement. (*b*)–(*e*) Spatial distributions of the absorption coefficient of the naturally grown a-TiO₂ single crystal taken at photon energies of 534.2 eV and 458.4 eV. The sample orientation and the scan range are the same as that for the PES measurement (Fig. 11). The scan interval was set to 0.25 mm. The image was mapped with an acquisition time of ∼25 min. The spectra were obtained by measuring the sample drain current [(*b*) and (*c*)] or by counting the photoelectrons that were emitted in the grazing direction [(*d*) and (*e*)]. The bold lines in panels (*b*)–(*e*) show the spectral intensities along the same spatial line as the one measured by the PES [black line in Fig. 11(*b*)]. The images were taken at room temperature.

beam size was larger than that (130 µm) calculated through a ray-tracing simulation (Mase *et al.*, 2010). The unexpected broadening of the beam size at photon energies of 100 eV and 1000 eV is considered to be caused by the slope error owing to an increase in thermal load on the pre-focusing mirror installed in the uppermost stream of the beamline near the lower and upper photon energies (Toyoshima *et al.*, 2011). The ES size was proportional to the vertical beam size but it did not affect the horizontal one. Since the beam position did not reproduce before and after operating the undulator magnets, the observed fluctuation in the beam position with the photon energy and polarization state is presumed to be owing to the extrinsic factors, such as the mechanical reproducibility of the undulator magnets and the heat load on the monochromator. Our results suggest the need for a detector that can easily estimate the position of the beam profile to perform microscopic measurements using the synchrotron radiation. To demonstrate the performance/usefulness of the microscopic system incorporating the HP-*XYZ* translator, we investigated the homogeneities in an SnO film and a naturally grown a-TiO₂ single crystal. In the SnO film, the spatial distribution of the absorption coefficient at a constant photon energy showed

that there are many voids in the order of 100 µm. Moreover, the microscopic XAS results showed that the constitutional element (Sn and O) concentrations in the voids were less than those in the homogeneous region. The other example to demonstrate the usefulness is an observation of the inherent impurities in a naturally grown a-TiO₂ single crystal. The scanning PES/XAS spectra showed the presence of impurities at the same location inside the homogeneous/stoichiometric sample. From the scanning XAS measurements with different surface sensitivities, it was suggested that the impurities are intrinsic in the bulk. Through the application of the SnO film and naturally grown a-TiO₂ single crystal, we showed that the upgraded apparatus at PF BL-13B incorporating the HP-*XYZ* translator can be used for microscopic elemental analyses and electronic structure studies. Since the position-control accuracy of the HP-*XYZ* translator exceeds the beam size, the spatial resolution of the VUV/SX microspectroscopy at PF BL-13B is determined by the beam size.

The following is a discussion on upgrading the microspectroscopy system at PF BL-13B. As mentioned in the introduction, to enable microscopic measurements using synchrotron radiation, it is indispensable not only to improve

the precise control of sample position but also to reduce the beam spot size at the sample position. This report focuses on the former task. The PF BL-13B covers photon energies ranging from 30 to 1600 eV. Except for a photon energy of ~400 eV, the beam size in the horizontal plane is considerably over 100 μm at the sample position (in Fig. 6, 216 μm for $h\nu$ = 100 eV and 221 μm for $h\nu$ = 1000 eV). In state-of-the-art micrometre-spectroscopic systems without any focusing zone plate, the beam size of VUV/SX is less than 50 μm along the horizontal direction at the sample position (Rotenberg & Bostwick, 2014; Jacobsen, 2019; Hoesch et al., 2017). Recently, we re-calculated the beam profiles using the ray-tracing simulation in detail, and the beam size in the lateral direction could be significantly reduced by changing the magnification of the focusing mirror from 1:1 to a higher magnification. To reduce the beam size of VUV/SX at PF BL-13B, we will upgrade the monochromator based on the ray-tracing simulation.

Acknowledgements

Funding information

References

Aiura, Y., Bando, H., Miyamoto, T., Chiba, A., Kitagawa, R., Maruyama, S. & Nishihara, Y. (2003). Rev. Sci. Instrum. **74**, 3177–3179.
Aiura, Y. & Kitano, K. (2012). Rev. Sci. Instrum. **83**, 035106.
Amemiya, K. (2012). Phys. Chem. Chem. Phys. **14**, 10477–10484.
Avila, J., Razado-Colambo, I., Lorcy, S., Giorgetta, J.-L., Polack, F. & Asensio, M. C. (2013). J. Phys. Conf. Ser. **425**, 132013.
Damascelli, A., Hussain, Z. & Shen, Z.-X. (2003). Rev. Mod. Phys. **75**, 473–541.
Dudin, P., Lacovig, P., Fava, C., Nicolini, E., Bianco, A., Cautero, G. & Barinov, A. (2010). J. Synchrotron Rad. **17**, 445–450.
Fujita, N. & Mase, K. (2007). J. Vac. Soc. Jpn. **50**, 583–585.
Fukuda, K. & Someya, T. (2017). Adv. Mater. **29**, 1602736.
Grätzel, M. (2009). Acc. Chem. Res. **42**, 1788–1798.
Günther, S. (2002). Prog. Surf. Sci. **70**, 187–260.
Hoesch, M., Kim, T. K., Dudin, P., Wang, H., Scott, S., Harris, P., Patel, S., Matthews, M., Hawkins, D., Alcock, S. G., Richter, T., Mudd, J. J., Basham, M., Pratt, L., Leicester, P., Longhi, E. C., Tamai, A. & Baumberger, F. (2017). Rev. Sci. Instrum. **88**, 013106.
Hüfner, S. (2003). Photoelectron Spectroscopy – Principles and Applications. Berlin: Springer-Verlag.
Hüfner, S. (2007). Very High Resolution Photoelectron Spectroscopy. Berlin: Springer-Verlag.
Iwasawa, H., Dudin, P., Inui, K., Masui, T., Kim, T. K., Cacho, C. & Hoesch, M. (2019). Phys. Rev. B, **99**, 140510.
Iwasawa, H., Schwier, E. F., Arita, M., Ino, A., Namatame, H., Taniguchi, M., Aiura, Y. & Shimada, K. (2017b). Ultramicroscopy, **182**, 85–91.
Iwasawa, H., Shimada, K., Schwier, E. F., Zheng, M., Kojima, Y., Hayashi, H., Jiang, J., Higashiguchi, M., Aiura, Y., Namatame, H. & Taniguchi, M. (2017a). J. Synchrotron Rad. **24**, 836–841.
Iwasawa, H., Takita, H., Goto, K., Mansuer, W., Miyashita, T., Schwier, E. F., Ino, A., Shimada, K. & Aiura, Y. (2018). Sci. Rep. **8**, 17431.
Jacobsen, C. (2019). X-ray Microscopy. Cambridge University Press.
Kondo, T., Khasanov, R., Karpinski, J., Kazakov, S. M., Zhigadlo, N. D., Ohta, T., Fretwell, H. M., Palczewski, A. D., Koll, J. D., Mesot, J., Rotenberg, E., Keller, H. & Kaminski, A. (2007). Phys. Rev. Lett. **98**, 157002.
Lee, C.-C., Yoshinobu, J., Mukai, K., Yoshimoto, S., Ueda, H., Friedlein, R., Fleurence, A., Yamada-Takamura, Y. & Ozaki, Y. (2017). Phys. Rev. B, **95**, 115437.
Lee, J., Park, C., Song, I., Koo, J. Y., Yoon, T., Kim, J. S. & Choi, H. C. (2018). Sci. Rep. **8**, 7617.
Liu, R.-Y., Ozawa, K., Terashima, N., Natsui, Y., Feng, B., Ito, S., Chen, W.-C., Cheng, C.-M., Yamamoto, S., Kato, H., Chiang, T.-C. & Matsuda, I. (2018). Appl. Phys. Lett. **112**, 211603.
Lupi, S., Baldassarre, L., Mansart, B., Perucchi, A., Barinov, A., Dudin, P., Papalazarou, E., Rodolakis, F., Rueff, J.-P., Itié, J.-P., Ravy, S., Nicoletti, D., Postorino, P., Hansmann, P., Parragh, N., Toschi, A., Saha-Dasgupta, T., Andersen, O. K., Sangiovanni, G., Held, K. & Marsi, M. (2010). Nat. Commun. **1**, 105.
Mase, K., Toyoshima, A., Kikuchi, T., Tanaka, H., Amemiya, K., Ito, K., Garrett, R., Gentle, I., Nugent, K. & Wilkins, S. (2010). AIP Conf. Proc. **1234**, 709–712.
McLeod, J. A., Skorikov, N. A., Finkelstein, L. D., Kurmaev, E. Z. & Moewes, A. (2012). J. Phys. Chem. C, **116**, 24248–24254.
Minohara, M., Kikuchi, N., Yoshida, Y., Kumigashira, H. & Aiura, Y. (2019). J. Mater. Chem. C. **7**, 6332–6336.
Minohara, M., Samizo, A., Kikuchi, N., Bando, K. K., Yoshida, Y. & Aiura, Y. (2020). J. Phys. Chem. C, **124**, 1755–1760.
Ozawa, K., Munakata, S., Edamoto, K. & Mase, K. (2011). J. Phys. Chem. C, **115**, 21843–21851.
Ozawa, K., Yamamoto, S., Yukawa, R., Liu, R.-Y., Terashima, N., Natsui, Y., Kato, H., Mase, K. & Matsuda, I. (2018). J. Phys. Chem. C, **122**, 9562–9569.
Picone, A., Riva, M., Brambilla, A., Calloni, A., Bussetti, G., Finazzi, M., Ciccacci, F. & Duò, L. (2016). Surf. Sci. Rep. **71**, 32–76.
Powell, C. J. (1988). J. Electron Spectrosc. Relat. Phenom. **47**, 197–214.
Quackenbush, N. F., Allen, J. P., Scanlon, D. O., Sallis, S., Hewlett, J. A., Nandur, A. S., Chen, B., Smith, K. E., Weiland, C., Fischer, D. A., Woicik, J. C., White, B. E., Watson, G. W. & Piper, L. F. J. (2013). Chem. Mater. **25**, 3114–3123.
Rotenberg, E. & Bostwick, A. (2014). J. Synchrotron Rad. **21**, 1048–1056.
Sharma, V., Vyas, R., Bazylewski, P., Chang, G. S., Asokan, K. & Sachdev, K. (2016). RSC Adv. **6**, 29135–29141.
Sumi, N., Yamada, Y., Sasaki, M., Arafune, R., Takagi, N., Yoshizawa, S. & Uchihashi, T. (2019). J. Phys. Chem. C, **123**, 8951–8958.
Toyoshima, A., Kikuchi, T., Tanaka, H., Mase, K., Amemiya, K. & Ozawa, K. (2013). J. Phys. Conf. Ser. **425**, 152019.
Toyoshima, A., Tanaka, H., Kikuchi, T., Amemiya, K. & Mase, K. (2011). J. Vac. Soc. Jpn. **54**, 580–584.
Zeradjanin, A. R., Menzel, N., Schuhmann, W. & Strasser, P. (2014). Phys. Chem. Chem. Phys. **16**, 13741–13747.
Zhang, C., Tsuboi, H., Hasegawa, Y., Iwasawa, M., Sasaki, M., Wakayama, Y., Ishii, H. & Yamada, Y. (2019). ACS Omega, **4**, 8669–8673.